Supplement of Atmos. Chem. Phys., 22, 273–293, 2022
https://doi.org/10.5194/acp-22-273-2022-supplement

Atmospheric Chemistry and Physics
Open Access

Supplement of

Aqueous secondary organic aerosol formation from the direct photosensitized oxidation of vanillin in the absence and presence of ammonium nitrate

Brix Raphael Go et al.

Correspondence to: Chak K. Chan (chak.k.chan@cityu.edu.hk)

Section S1. Materials.

Initial solutions of 0.1 mM vanillin (VL, Acros Organics, 99%, pure), 0.1 mM guaiacol (GUA, Sigma Aldrich, ≥ 98.0%), 1 mM ammonium nitrate (AN, Acros Organics, 99+%, for analysis), and 1 mM sodium nitrate (SN, Sigma-Aldrich, ≥ 99.5%) were prepared in Milli-Q water. The pH values of the samples were adjusted using sulfuric acid (H_2SO_4; Acros Organics, ACS reagent, 95% solution in water).

Section S2. UV-Vis spectrophotometric analyses.

The absorbance changes for all samples were characterized using a UV-Vis spectrophotometer (UV-3600, Shimadzu Corp., Japan). The absorbance values from 200 to 700 nm were recorded instantly after sample collection, and measurements were done in triplicate. Absorbance enhancements were calculated as the change in the integrated area of absorbance from 350 to 550 nm. The increase of light absorption at this wavelength range, where VL and GUA did not initially absorb light, suggests the formation of light-absorbing compounds (Zhou et al., 2019).

Section S3. UHPLC-PDA analyses.

An ultra-high performance liquid chromatography system (UHPLC, Waters Acquity H-Class, Waters, Milford, USA) coupled to a photodiode array (PDA) detector (Waters, Milford, USA) was used for the quantification of VL and GUA concentrations. The drawn solutions were first filtered through a 0.2 μm Chromafil ®Xtra PTFE filter (Macherey-Nagel GmbH & Co. KG, Germany). Briefly, the separation of products was performed using an Acquity HSS T3 column (1.8 μm, 2.1 mm × 100 mm; Waters Corp.). The column oven was held at 30 ºC, and the autosampler was cooled at 4 ºC. The injection volume was set to 5 μL. The binary mobile phase consisted of A (water) and B (acetonitrile). The gradient elution was performed at a flow rate of

0.2 mL/min: 0–1 min, 10% eluent B; 1–25 min, linear increase to 90% eluent B; 25–29.9 min, hold 90% eluent B; 29.9–30 min, decrease to 10% eluent B; 30–35 min, re-equilibrate at 10% eluent B for 5 min. Standard solutions of VL and GUA ranging from 10 to 130 μM were analyzed along with samples and blanks using the channels with UV absorption at 300 and 274 nm, respectively. The calibration curves for VL and GUA standard solutions are shown in Figure S2.

Section S4. IC analyses of small organic acids.

The small organic acids were analyzed using an ion chromatography system (IC, Dionex ICS-1100, Sunnyvale, CA) equipped with a Dionex AS-DV autosampler (Sunnyvale, CA). The separation was achieved using an IonPac™ AS15 column (4 × 250 mm) with an AG15 guard column (4 × 50 mm). The isocratic gradient was applied at a flow rate of 1.2 mL/min with 38 mM sodium hydroxide (NaOH) as the eluent. The total run time was set at 20 min. The standard solutions (1–50 μM) of formic, succinic, and oxalic acid were analyzed three times along with the samples and water blank. Formic, succinic, and oxalic acid had retention times of 3.6 min, 8.3 min, and 11.9 min, respectively.

Section S5. UHPLC-qToF-MS analyses.

The characterization of reaction products was performed using a UHPLC system (ExionLC™ AD, ABSciex, Concord, Canada) coupled to a quadrupole time-of-flight mass spectrometer (qToF-MS) (TripleTOF 6600+, ABSciex). The settings (e.g., column, mobile phase, gradient, oven temperature) in the UHPLC system were the same as those used in UHPLC-PDA (Section S3). The mass spectrometer was equipped with an electrospray ionization (ESI) source and operated in the positive ion mode (the negative ion mode signals were too low for our analyses) at a resolving power (full width at half-maximum (fwhm) at m/z 300) of 30000 in MS and 30000

in MS/MS (high-resolution mode). Information-dependent acquisition (IDA) scanning was adapted for product identification. The acquisition using IDA consisted of a ToF-MS scan and information-dependent trigger events. The ToF-MS scan had an accumulation time of 250 ms and covered a mass range of m/z 30–700 with a declustering potential (DP) of 40 and collision energy (CE) of 10 eV. The accumulation time for the IDA experiment was 100 ms, and the MS/MS scan range was set from m/z 30–700 in high-resolution mode. The IDA criteria were as follows: 5 most intense ions (number of IDA experiments) with an intensity threshold above 50 cps, isotope exclusion was switched off, and dynamic background subtraction was switched on. The automated calibration device system (CDS) was set to perform an external calibration every four samples. The ESI source conditions were as follows: temperature, 500 °C; curtain gas (CUR), 25 psi; ion source gas 1 at 50 psi; ion source gas 2 at 50 psi; and ion-spray voltage floating (ISVF) at 4.5 kV.

All parameters in the liquid chromatography system and mass spectrometer were controlled using Analyst TF Software 1.8 (ABSciex). The high-resolution LC-MS data were processed with PeakView and Analyst in the SCIEX OS software 1.5 (ABSciex). Peaks from the blank sample were subtracted from the sample signals. In addition to a minimum signal-to-noise ratio of 30, a peak was determined as a product if the difference in peak area between the samples before and after irradiation is ≥ 10 times. The formula assignments were carried out using the MIDAS molecular formula calculator (http://magnet.fsu.edu/~midas/) with the following constraints: C ≤ 35, H ≤ 70, N ≤ 5, O ≤ 20, Na ≤ 1, and the mass error was initially set at 10 ppm. The nitrogen atom was removed in the constraints for the experiments without AN or SN. The detected adducts in ESI positive ion mode have several types (e.g., $[M+H]^+$, $[M+Na]^+$), and their formation can be influenced by the sample matrix (Erngren et al., 2019). For simplification purposes, we mainly considered $[M+H]^+$ adducts for formula assignments, except for specific experiments with AN or

SN in which $[M+NH_4]^+$ adducts and $[M+Na]^+$ adducts were observed. The final assigned formulas were constrained by a mass error of mostly < 5 ppm, which is a requirement for product identification using positive ion mode (Roemmelt et al., 2015). The double bond equivalent (DBE) values and carbon oxidation state (OS_c) of the neutral formulas were calculated using the following equations (Koch and Dittmar, 2006):

$$DBE = C - H/2 + N/2 + 1 \quad \text{(Eq. S1)}$$

$$OS_c = 2 \times O/C - H/C \quad \text{(Eq. S2)}$$

where C, H, O, and N correspond to the number of carbon, hydrogen, oxygen, and nitrogen atoms in the neutral formula, respectively. Based on the detected products, the average oxygen to carbon (O:C) ratios, ⟨O:C⟩ : ($\langle O{:}C \rangle = \sum_i (\text{abundance}_i) O_i / \sum_i (\text{abundance}_i) C_i$) and average hydrogen to carbon (H:C) ratios, ⟨H:C⟩: ($\langle H{:}C \rangle = \sum_i (\text{abundance}_i) H_i / \sum_i (\text{abundance}_i) C_i$) after the reactions were further estimated using the signal-weighted method (Bateman et al., 2012). The average OS_c $\langle OS_c \rangle$, was calculated as follows:

$$\langle OS_c \rangle = 2 \times \langle O{:}C \rangle - \langle H{:}C \rangle \quad \text{(Eq. S3)}$$

Based on the typical MS/MS fragmentation behavior for individual functional groups (Table S1) and DBE values, examples of structures for products detected from VL (and GUA) photo-oxidation experiments were proposed (Table S2).

Section S6. Photon flux measurements.

In this work, 2-nitrobenzaldehyde (2NB), a chemical actinometer, was used to determine the photon flux in the aqueous photoreactor. Briefly, the photolysis of 50 μM 2NB in the reactor was monitored by determining its concentration every 5 min for a total of 35 min, during which

2NB was almost completely decayed. The concentration of 2NB was measured using UHPLC-PDA, and the settings (e.g., column, mobile phase, gradient, oven temperature) were the same as those for VL decay analysis (Section S3). The channel with UV absorption at 254 nm was used for the quantification of 2NB. The concentration of 2NB in the reactor followed exponential decay, and its decay rate constant was determined using the following equation:

$$ln\left(\frac{[\mathrm{2NB}]_t}{[\mathrm{2NB}]_0}\right) = -j(\mathrm{2NB}) \times t \qquad \text{(Eq. S4)}$$

where $[\mathrm{2NB}]_t$ and $[\mathrm{2NB}]_0$ are the 2NB concentrations at time t and 0, respectively. The calculated 2NB decay rate constant, j(2NB), was 0.0026 s^{-1}. The following equation can also be used to calculate j(2NB):

$$j(\mathrm{2NB}) = 2.303 \times (10^3\ \mathrm{cm}^3\ \mathrm{L}^{-1} \times\ 1\ \mathrm{mol/N_A\ mlc}) \times \sum\left(I'_\lambda \times \Delta\lambda \times \varepsilon_{\mathrm{2NB},\lambda} \times \Phi_{\mathrm{2NB}}\right) \qquad \text{(Eq. S5)}$$

where N_A is Avogadro's number, I'_λ is the actinic flux (photons cm^{-2} s^{-1} nm^{-1}), $\Delta\lambda$ is the wavelength interval between actinic flux data points (nm), and $\varepsilon_{\mathrm{2NB},\lambda}$ and $\Phi_{\mathrm{2NB},\lambda}$ are the base-10 molar absorptivity (M^{-1} cm^{-1}) and quantum yield (molecule $photon^{-1}$) for 2NB, respectively. Values of $\varepsilon_{2NB,\lambda}$ (in water) at each wavelength under 298 K and a wavelength-independent Φ_{2NB} value of 0.41 were adapted from Galbavy et al. (2010). Similar to Smith et al. (2014, 2016), we measured the spectral shape of the photon output of our illumination system (i.e., the relative flux at each wavelength) using a high-sensitivity spectrophotometer (Brolight Technology Co. Ltd, Hangzhou, China). Using a scaling factor (SF), this measured relative photon output, $I_\lambda^{\mathrm{relative}}$, is related to I'_λ as follows (Hullar et al., 2020):

$$I'_\lambda = I_\lambda^{\mathrm{relative}} \times \mathrm{SF} \qquad \text{(Eq. S6)}$$

Substitution of Eq. S6 into Eq. S5 and rearrangement yields:

$$\mathrm{SF} = \frac{j(\mathrm{2NB})}{2.303 \times (10^3\ \mathrm{cm^3\ L^{-1}} \times 1\ \mathrm{mol/N_A\ mlc}) \times \sum\left(I_\lambda^{\mathrm{relative}} \times \Delta\lambda \times \varepsilon_{\mathrm{2NB},\lambda} \times \Phi_{\mathrm{2NB}}\right)} \qquad \text{(Eq. S7)}$$

and substitution of Eq. S6 into Eq. S7 yields:

$$I'_\lambda = I_\lambda^{\mathrm{relative}} \frac{j(\mathrm{2NB})}{2.303 \times (10^3\ \mathrm{cm^3\ L^{-1}} \times 1\ \mathrm{mol/N_A\ mlc}) \times \sum\left(I_\lambda^{\mathrm{relative}} \times \Delta\lambda \times \varepsilon_{\mathrm{2NB},\lambda} \times \Phi_{\mathrm{2NB}}\right)} \qquad \text{(Eq. S8)}$$

Finally, I'_λ was estimated through Eq. S8. The estimated photon flux in the aqueous reactor is shown in Fig. S1. The actinic flux during a haze event over Beijing (40º N, 116º E) on January 12, 2013, at 12:00 pm (GMT+8) (Che et al., 2014) estimated using the National Center for Atmospheric Research Tropospheric Ultraviolet-Visible (TUV) Radiation Model (http://cprm.acom.ucar.edu/Models/TUV/Interactive_TUV/) is also shown in Figure S2. The parameters used for the Quick TUV calculator were: Overhead Ozone Column: 300 du; Surface Albedo: 0.1; Ground Elevation: 0 km asl; Measured Altitude: 0 km asl; Clouds optical depth: 0, base: 4, top: 5; Aerosols optical depth: 2.5, single scattering albedo: 0.9, Angstrom exponent: 1; Sunlight direct beam, diffuse down, diffuse up: 1; 4 streams transfer model. For clear days, the actinic flux was estimated over Beijing (at the same date and time) using the default parameters.

Table S1. Typical fragmentation behavior observed in MS/MS spectra for individual functional groups from Holčapek et al. (2010).

Functional group	**Fragment ions**	**MS/MS loss**
Nitro (RNO_2)	$[M+H-OH]^{+\bullet}$	-OH
	$[M+H-H_2O]^+$	$-H_2O$
	$[M+H-NO]^{+\bullet}$	-NO
	$[M+H-NO_2]^{+\bullet}$	$-NO_2$
Nitroso (RNO)	$[M+H-NO]^+$	-NO
Carboxylic acid (ROOH)	$[M+H-H_2O]^+$	$-H_2O$
	$[M+H-CO_2]^+$	$-CO_2$
	$[M+H-H_2O-CO]^+$	$-H_2O-CO$
Phenol (ROH)	$[M+H-H_2O]^+$	$-H_2O$
	$[M+H-CO]^+$	-CO
Methoxy ($ROCH_3$)	$[M+H-CH_3]^{+\bullet}$	$-CH_3$
	$[M+H-CH_3O]^{+\bullet}$	$-CH_3O$
	$[M+H-CH_3OH]^+$	$-CH_3OH$
	$[M+H-HCOH]^+$	-HCOH
Ester (R^1COOR^2)	$[M+H-R^2OH]^+$	$-R^2OH$
	$[M+H-R^2OH-CO]^+$	$-R^2OH-CO$
Amine	$[M+H-NH_3]^+$	$-NH_3$
Aldehyde (RCHO)	$[M+H-CO]^+$	-CO

Table S2. Examples of proposed structures for products detected from vanillin (and guaiacol) photo-oxidation experiments in this study.

No.	Formula	DBE	Proposed structure	MS/MS fragment ions		
1	$C_8H_8O_3$ (VL; triplet and aqSOA precursor)	5	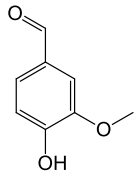	-CO-CH_3OH	-CO	-CO-CH_3OH-CO
2	$C_7H_8O_2$ (GUA; aqSOA precursor)	4	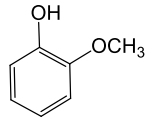			
3	$C_8H_9NO_3$	5	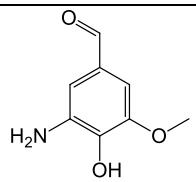	-CO-CH_3	-NH_3	
4	$C_{16}H_{10}N_2O_9$	13	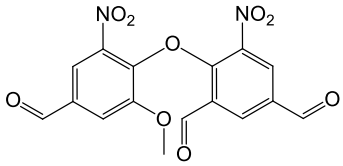	-NO_2		
5	$C_{10}H_{10}O_5$	6	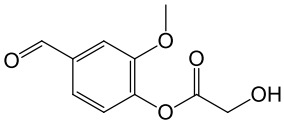	-CH_3OH	-CH_3OH-CO	
6	$C_5H_5N_3O_2$	5	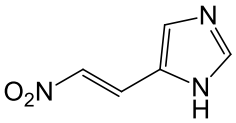	-NH		
7	$C_{16}H_{14}O_6$	10	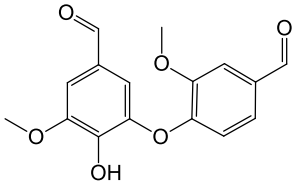	-CO-CH_3OH-CO	-CO-CH_3OH-CO-CH_3OH	-CO-CH_3OH-CO-CO
8	$C_7H_6O_3$	5	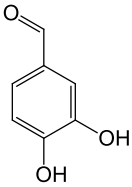			

9	$C_8H_8O_4$	5	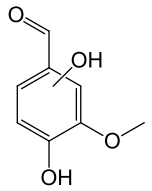	-CO-CH $_3$OH	-CO	-H_2O
10	$C_{15}H_{12}O_8$	10	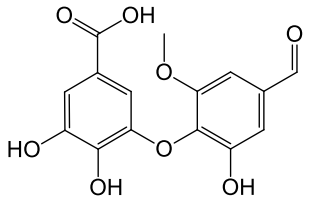	-COOH		
11	$C_7H_4N_2O_7$	7	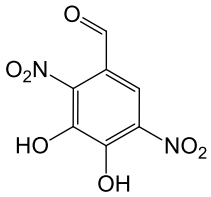			
12	$C_8H_6O_4$	6	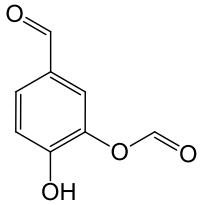	-CO	-CO-CO	
13	$C_{14}H_{14}O_4$	8	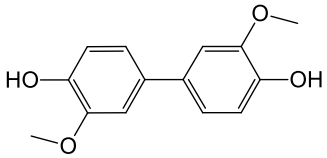			
14	$C_{21}H_{20}O_6$	12	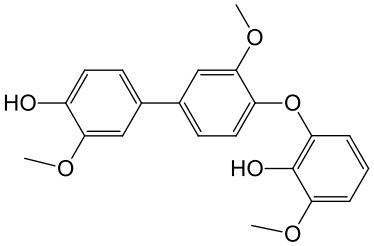			
15	$C_{28}H_{26}O_8$	16	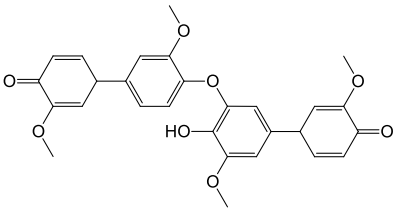			
16	$C_7H_4O_4$	6	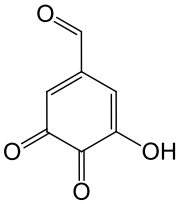	-CO	-CO-CO	

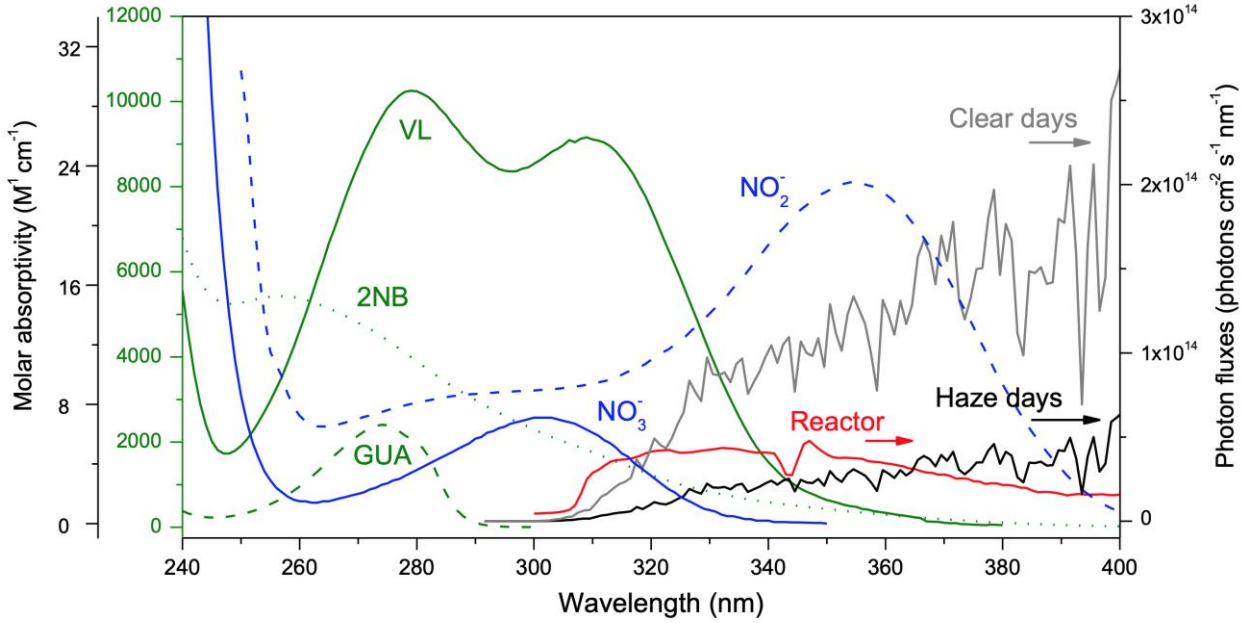

Figure S1. The base-10 molar absorptivities (ε, M^{-1} cm^{-1}) of vanillin (VL, green solid line), 2-nitrobenzaldehyde (2NB, green dotted line), guaiacol (GUA, green dashed line), NO_2^- (blue dashed line), NO_3^- (blue solid line), and photon flux in the aqueous reactor (red line) during typical haze days (black line) or clear days (gray line) in Beijing, China. The ε values for 2NB and NO_2^- were adapted from Galbavy et al. (2010) and Chu and Anastasio (2007), respectively.

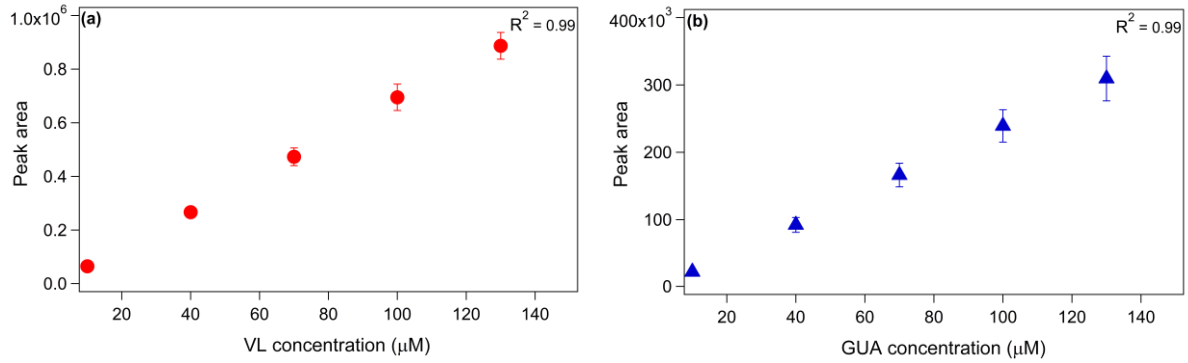

Figure S2. Calibration curves for **(a)** VL and **(b)** GUA standard solutions (10–130 μM). Error bars represent 1 standard deviation.

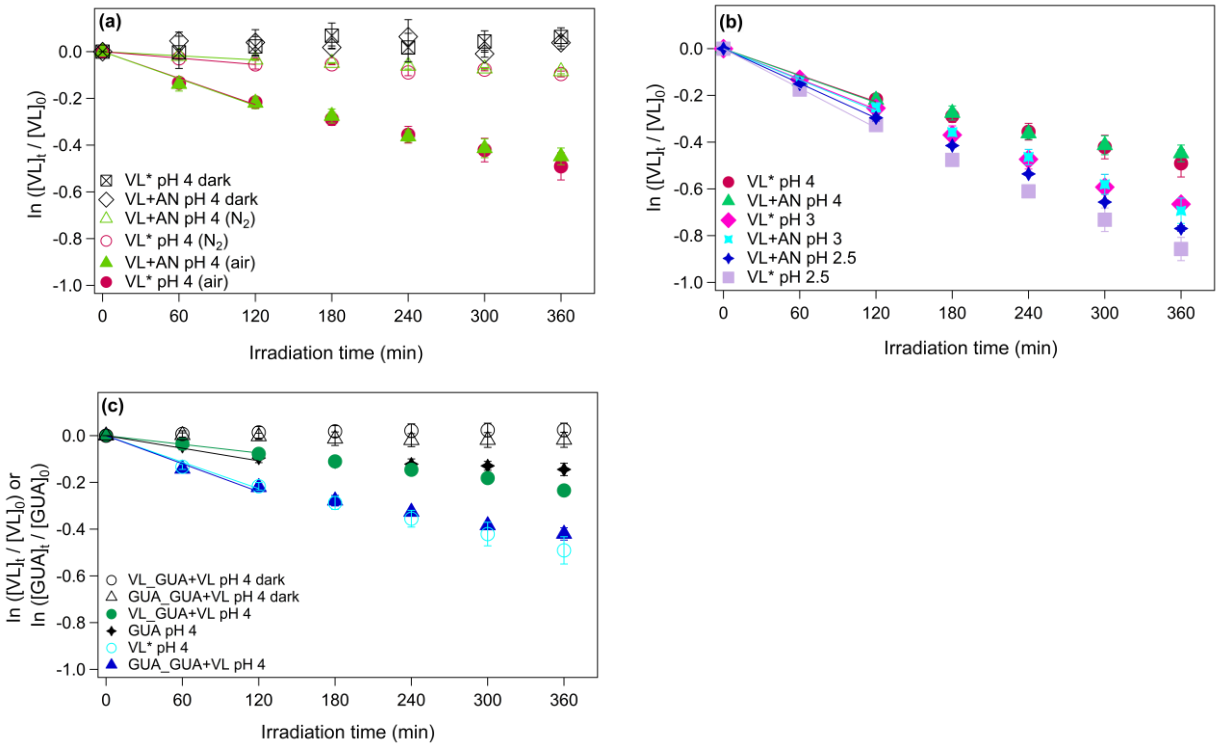

Figure S3. (a–c) The decay of VL under different experimental conditions for direct photosensitized oxidation of VL in the absence (VL*) and presence of ammonium nitrate (VL+AN): **(a)** VL* and VL+AN at pH 4 under N_2– (A6 and A8) and air-saturated (A5 and A7) conditions. No statistically significant difference ($p > 0.05$) was noted between VL+AN (A7) and VL+SN (A9; not shown here). **(b)** Effect of pH on VL* and VL+AN at pH 2.5 (A1 and A2), 3 (A3 and A4), and 4 (A5 and A7) under air-saturated conditions. **(c)** The decay of VL (and GUA) during direct GUA photodegradation (A13) and oxidation of GUA via photosensitized reactions of VL (GUA+VL; A14) at pH 4 under air-saturated conditions after 6 h of simulated sunlight irradiation. Error bars represent 1 standard deviation; most error bars are smaller than the markers.

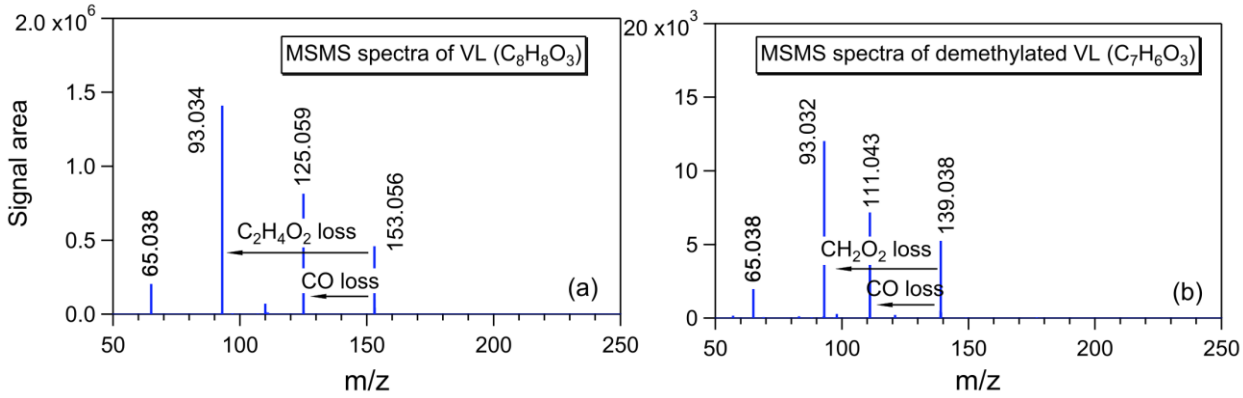

Figure S4. MS/MS spectra of **(a)** VL and **(b)** demethylated VL. The arrows indicate possible fragmentation pathways of VL and demethylated VL.

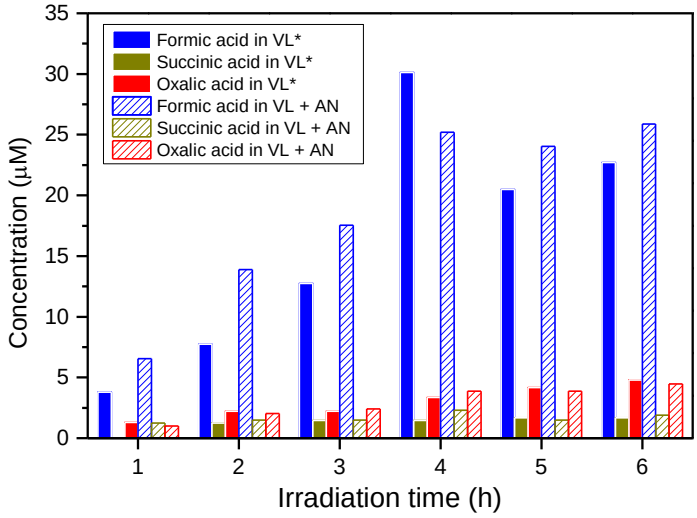

Figure S5. The concentration of formic, oxalic, and succinic acid at different reaction times for VL* (A5) and VL+AN (A7) at pH 4 under air-saturated conditions.

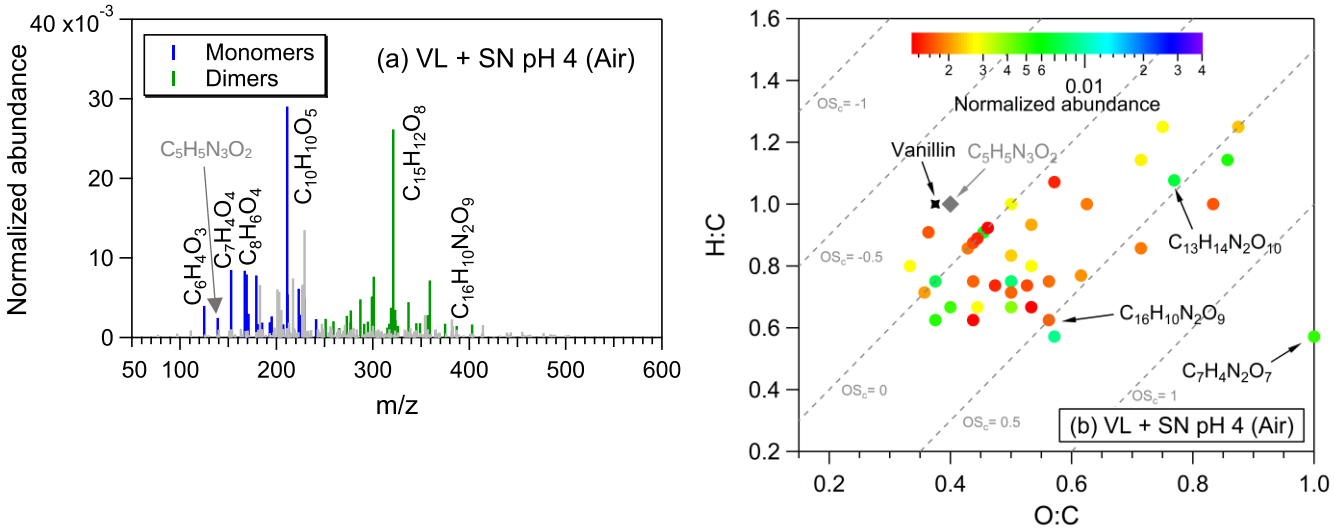

Figure S6. (a) Reconstructed mass spectra of assigned peaks and **(b)** Van Krevelen diagram of the 50 most abundant products from VL+SN (A9) at pH 4 under air-saturated conditions after 6 h of simulated sunlight irradiation. The normalized abundance of products was calculated using Eq. 2. The 50 most abundant products contributed more than half of the total normalized abundance of products, and they were identified as monomers (blue) and dimers (green). Gray peaks denote peaks with low abundance or unassigned formula. The gray arrows show where the potential imidazole derivative ($C_5H_5N_3O_2$) from VL+AN (A7) was observed. Examples of high-intensity peaks were labeled with the corresponding neutral formulas. The color bar denotes the normalized abundance of products. The gray dashed lines indicate the carbon oxidation state values (e.g., OS_c = -1, 0, and 1).

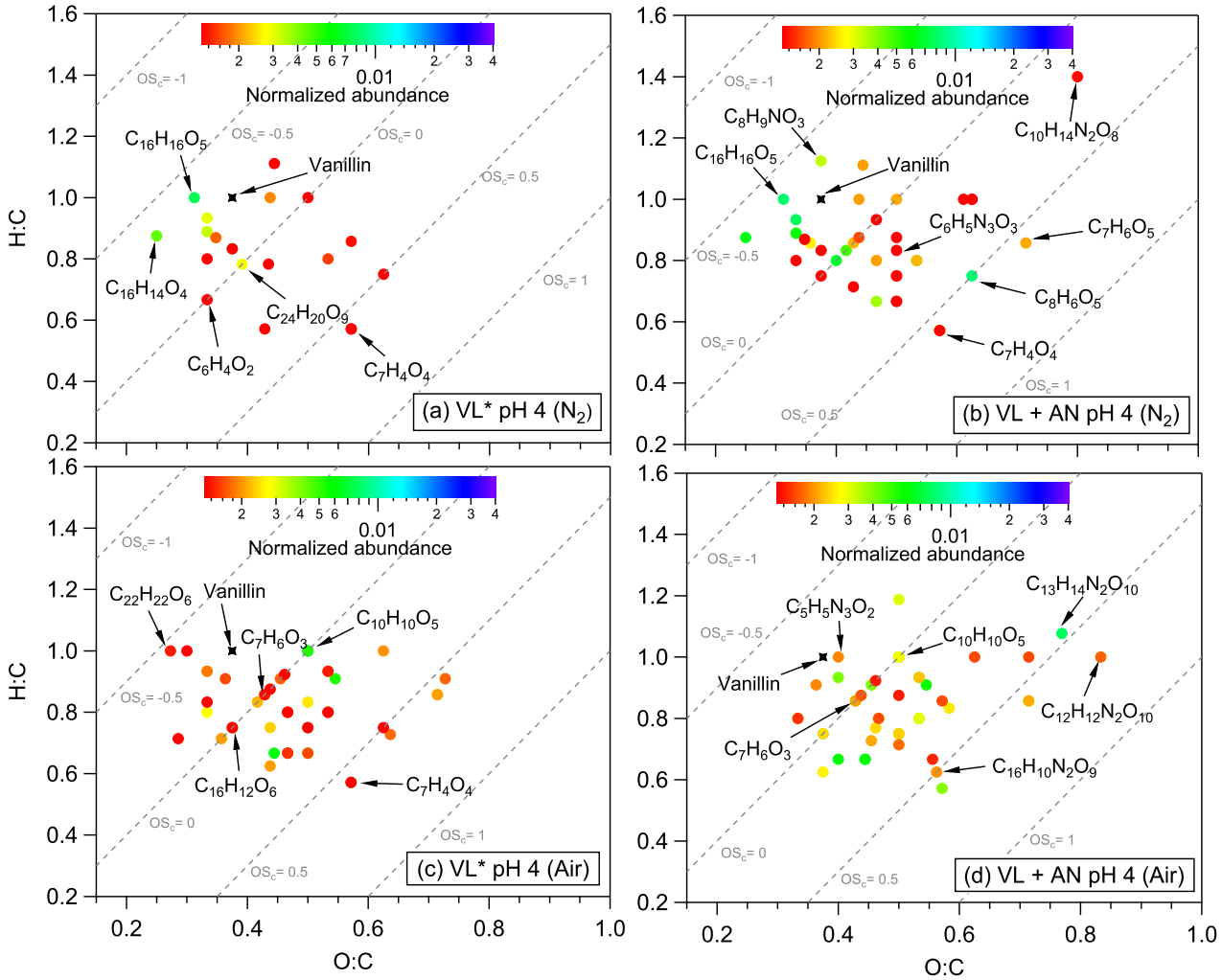

Figure S7. Van Krevelen diagrams of the 50 most abundant products from **(a)** VL* (N_2-saturated; A6), **(b)** VL+AN (N_2-saturated; A8), **(c)** VL* (air-saturated; A5), and **(d)** VL+AN (air-saturated; A7) at pH 4 after 6 h of simulated sunlight irradiation. The color bar denotes the normalized abundance of products. The gray dashed lines indicate the carbon oxidation state values (e.g., OS_c = -1, 0, and 1).

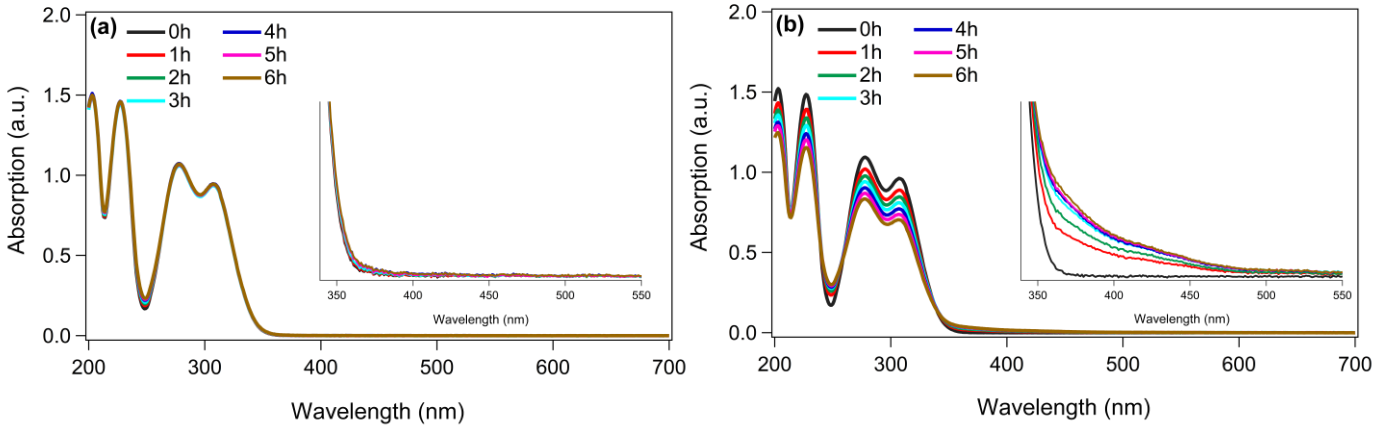

Figure S8. UV–Vis absorption spectra of VL* (A6 and A5; pH 4) under **(a)** N_2− and **(b)** air-saturated conditions at different time intervals. The insets show the absorbance enhancement from 350 to 550 nm.

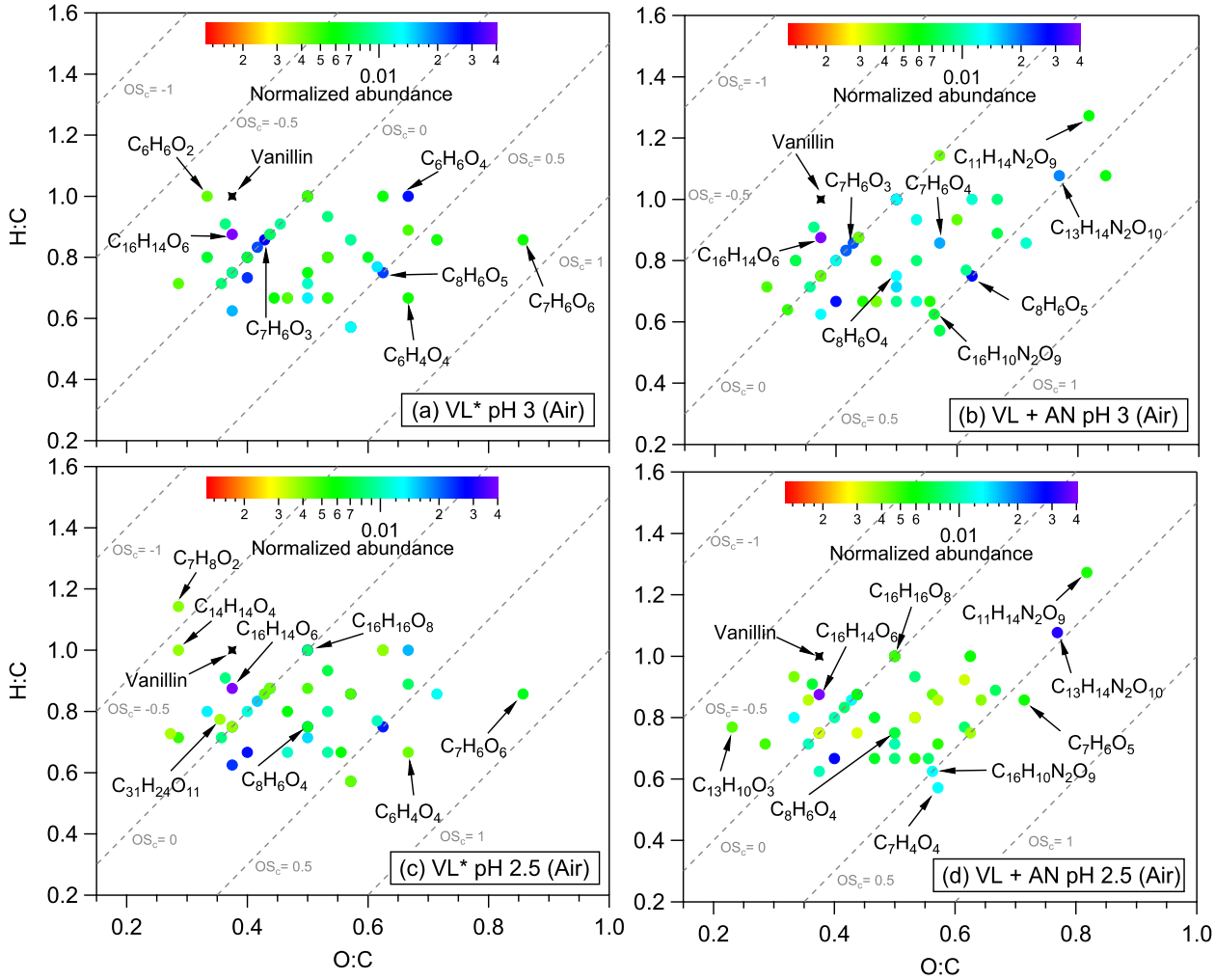

Figure S9. Van Krevelen diagrams of the 50 most abundant products from **(a)** VL* pH 3 (A3), **(b)** VL+AN pH 3 (A4), **(c)** VL* pH 2.5 (A1), and **(d)** VL+AN pH 2.5 (A2) under air-saturated conditions after 6 h of simulated sunlight irradiation. The color bar denotes the normalized abundance of products. The gray dashed lines indicate the carbon oxidation state values (e.g., OS_c =-1, 0, and 1).

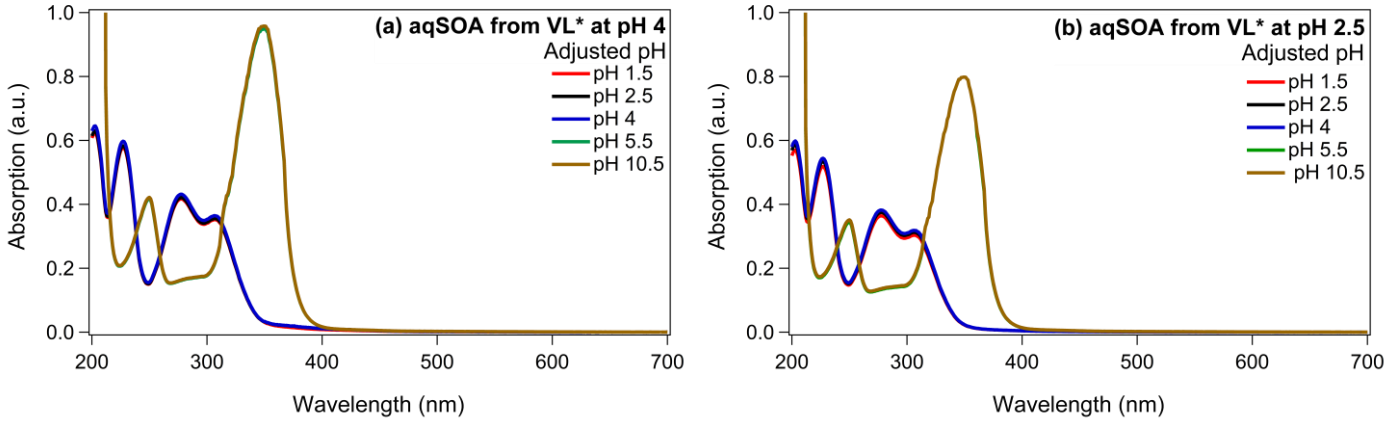

Figure S10. UV–Vis absorption spectra of VL*-derived aqSOA formed at **(a)** pH 4 and **(b)** pH 2.5 over a range of pH conditions from 1.5 to 10.5.

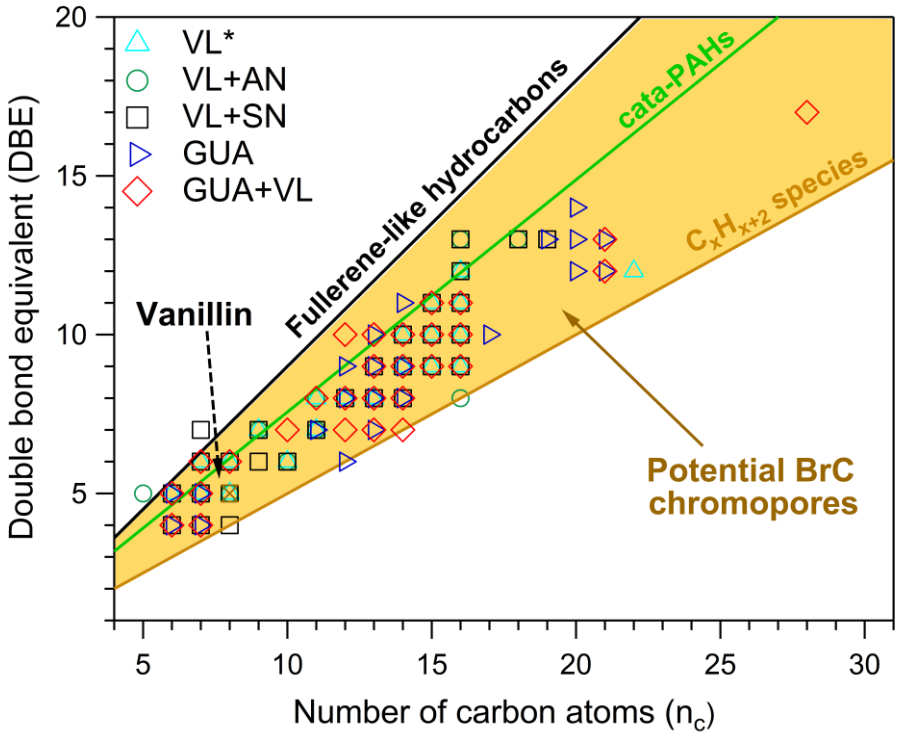

Figure S11. The plot of the double bond equivalent (DBE) values vs. number of carbon atoms (n_C) (Lin et al., 2018) for the 50 most abundant products from pH 4 experiments under air-saturated conditions. Dashed lines indicate DBE reference values of fullerene-like hydrocarbons (black solid line; Lobodin et al., 2012), cata-condensed polycyclic aromatic hydrocarbons (PAHs) (green solid line; Siegmann and Sattler, 2000), and linear conjugated polyenes (general formula C_xH_{x+2}) (brown solid line). Data points within the shaded area are potential BrC chromophores.

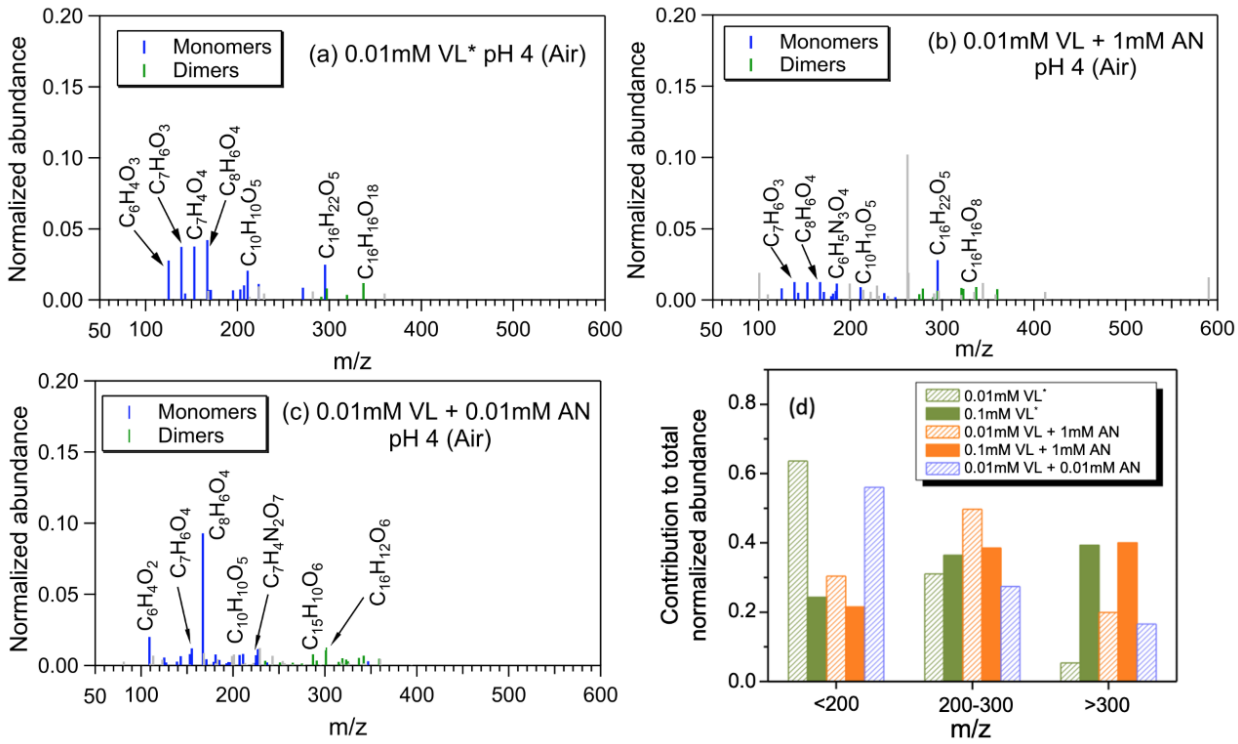

Figure S12. Reconstructed mass spectra of assigned peaks from **(a)** 0.01 mM VL* (A10), **(b)** 0.01 mM VL + 1 mM AN (A12), and **(c)** 0.01 mM VL + 0.01 mM AN (A11) at pH 4 under air-saturated conditions after 6 h of simulated sunlight irradiation. The normalized abundance of products was calculated using Eq. 2. The 50 most abundant products contributed more than half of the total normalized abundance of products, and they were identified as monomers (blue) and dimers (green). Gray peaks denote peaks with low abundance or unassigned formula. Examples of high-intensity peaks were labeled with the corresponding neutral formulas. **(d)** Contributions of different m/z ranges to the normalized abundance of products from experiments with low [VL] = 0.01 mM (A10–A12) and high [VL] = 0.1 mM (A5 and A7) at pH 4 under air-saturated conditions after 6 h of simulated sunlight irradiation.

References

Bateman, A. P., Laskin, J., Laskin, A., and Nizkorodov, S. A.: Applications of high-resolution electrospray ionization mass spectrometry to measurements of average oxygen to carbon ratios in secondary organic aerosols, Environ. Sci. Technol., 46, 8315–8324, https://doi.org/10.1021/es3017254, 2012.

Che, H., Xia, X., Zhu, J., Li, Z., Dubovik, O., Holben, B., Goloub, P., Chen, H., Estelles, V., Cuevas-Agulló, E., Blarel, L., Wang, H., Zhao, H., Zhang, X., Wang, Y., Sun, J., Tao, R., Zhang, X., and Shi, G.: Column aerosol optical properties and aerosol radiative forcing during a serious haze-fog month over North China Plain in 2013 based on ground-based sunphotometer measurements, Atmos. Chem. Phys., 14, 2125–2138, https://doi.org/10.5194/acp-14-2125-2014, 2014.

Chu, L. and Anastasio, C.: Temperature and wavelength dependence of nitrite photolysis in frozen and aqueous solutions, Environ. Sci. Technol., 41, 3626–3632, https://doi.org/10.1021/es062731q, 2007.

Erngren, I., Haglöf, J., Engskog, M. K. R., Nestor, M., Hedeland, M., Arvidsson, T., and Pettersson, C.: Adduct formation in electrospray ionisation-mass spectrometry with hydrophilic interaction liquid chromatography is strongly affected by the inorganic ion concentration of the samples, J. Chromatogr. A, 1600, 174–182, https://doi.org/10.1016/j.chroma.2019.04.049, 2019.

Galbavy, E. S., Ram, K., and Anastasio, C.: 2-Nitrobenzaldehyde as a chemical actinometer for solution and ice photochemistry, J. Photochem. Photobiol. A, 209, 186–192, https://doi.org/10.1016/j.jphotochem.2009.11.013, 2010.

Holčapek, M., Jirásko, R., and Lísa, M.: Basic rules for the interpretation of atmospheric pressure ionization mass spectra of small molecules, J. Chromatogr. A, 1217, 3908–3921, https://doi.org/10.1016/j.chroma.2010.02.049, 2010.

Hullar, T., Bononi, F. C., Chen, Z., Magadia, D., Palmer, O., Tran, T., Rocca, D., Andreussi, O., Donadio, D., and Anastasio, C.: Photodecay of guaiacol is faster in ice, and even more rapid on ice, than in aqueous solution, Environ. Sci.: Processes Impacts, 22, 1666–1677, https://doi.org/10.1039/d0em00242a, 2020.

Koch, B. P. and Dittmar, T.: From mass to structure: an aromaticity index for high-resolution mass data of natural organic matter, Rapid Commun. Mass Spectrom., 20, 926–932, https://doi.org/10.1002/rcm.2386 2006.

Lin, P., Fleming, L. T., Nizkorodov, S. A., Laskin, J., and Laskin, A.: Comprehensive molecular characterization of atmospheric brown carbon by high resolution mass spectrometry with electrospray and atmospheric pressure photoionization, Anal. Chem., 90, 12493–12502, https://doi.org/10.1021/acs.analchem.8b02177, 2018.

Lobodin, V. V., Marshall, A. G., and Hsu, C. S.: Compositional space boundaries for organic compounds, Anal. Chem., 84, 3410–3416, https://doi.org/10.1021/ac300244f, 2012.

Roemmelt, A. T., Steuer, A. E., and Kraemer, T.: Liquid chromatography, in combination with a quadrupole time-of-flight instrument, with sequential window acquisition of all theoretical fragment-ion spectra acquisition: validated quantification of 39 antidepressants in whole blood as part of a simultaneous screening and quantification procedure, Anal. Chem., 87, 9294–9301, https://doi.org/10.1021/acs.analchem.5b02031, 2015.

Siegmann, K. and Sattler, K.: Formation mechanism for polycyclic aromatic hydrocarbons in methane flames, J. Chem. Phys., 112, 698–709, https://doi.org/10.1063/1.480648, 2000.

Smith, J. D., Kinney, H., and Anastasio, C.: Phenolic carbonyls undergo rapid aqueous photodegradation to form low-volatility, light-absorbing products, Atmos. Environ., 126, 36−44, https://doi.org/10.1016/j.atmosenv.2015.11.035, 2016.

Smith, J. D., Sio, V., Yu, L., Zhang, Q., and Anastasio, C.: Secondary organic aerosol production from aqueous reactions of 973 atmospheric phenols with an organic triplet excited state, Environ. Sci. Technol., 48, 1049–1057, https://doi.org/10.1021/es4045715, 2014.

Zhou, W., Mekic, M., Liu, J., Loisel, G., Jin, B., Vione, D., and Gligorovski, S.: Ionic strength effects on the photochemical degradation of acetosyringone in atmospheric deliquescent aerosol particles, Atmos. Environ., 198, 83–88, https://doi.org/10.1016/j.atmosenv.2018.10.047, 2019.